

Large-Scale, Long-Time Atomistic Simulations of Proton Transport in Polymer Electrolyte Membranes Using a Neural Network Interatomic Potential

Yuta Yoshimoto, Naoki Matsumura, Yuto Iwasaki, Hiroshi Nakao, and Yasufumi Sakai*

Fujitsu Research, Fujitsu Limited, 4-1-1 Kamikodanaka, Nakahara-ku, Kawasaki, Kanagawa
211-8588, Japan

ABSTRACT

In recent years, machine learning interatomic potentials (MLIPs) have attracted significant attention as a method that enables large-scale, long-time atomistic simulations while maintaining accuracy comparable to electronic structure calculations based on density functional theory (DFT) and *ab initio* wavefunction theories. However, a challenge with MLIP-based molecular dynamics (MD) simulations is their lower stability compared to those using conventional classical potentials. Analyzing highly heterogeneous systems or amorphous materials often requires large-scale and long-time simulations, necessitating the development of robust MLIPs that allow for stable MD simulations. In this study, using our neural network potential (NNP) generator, we construct an NNP model that enables large-scale, long-time MD simulations of perfluorinated ionomer membranes (Nafion) across a wide range of hydration levels. We successfully build a robust deep potential (DP) model by iteratively expanding the dataset through active-learning loops. Specifically, by combining the sampling of off-equilibrium structures via non-equilibrium DPMD simulations with the structure screening in a 3D structural feature space incorporating minimum interatomic distances, it is possible to significantly enhance the robustness of the DP model, which allows for stable MD simulations of large Nafion systems ranging from approximately 10,000 to 20,000 atoms for an extended duration of 31 ns. The MD simulations employing the developed DP model yield self-diffusion coefficients of hydrogen atoms that more closely match experimental values in a wide range of hydration levels compared to previous *ab initio* MD simulations of smaller systems.

1. INTRODUCTION

Atomistic simulations using machine learning interatomic potentials (MLIPs) have garnered significant attention as a method capable of analyzing larger systems at the atomic level while maintaining accuracy comparable to electronic structure calculations.^{1–3} MLIPs, trained on datasets generated from electronic structure calculations such as density functional theory (DFT) or *ab initio* wavefunction theories, offer a more accurate representation of the multidimensional potential energy surface compared to traditional classical potentials. This allows for high-accuracy, long-time molecular dynamics (MD) simulations of large systems, which are intractable with electronic structure calculations. Thus far, various MLIPs have been proposed, including kernel-based potentials,^{4–7} neural network potentials (NNPs),^{8–13} and more sophisticated approaches based on graph neural networks^{14–22} and transformers.^{23–25} Their applications span a wide range of systems, including inorganic materials,^{26–30} molecular systems,^{9,10,31–34} solutions,^{35–38} polymeric materials,^{39–41} and interfacial systems,^{42,43} demonstrating the effectiveness of MLIPs across diverse systems.

While the application of MLIPs to material simulations is rapidly progressing, there are limited studies focusing on the stability of large-scale, long-time MLIP-MD simulations.^{44–46} Unlike conventional classical potentials, typical atom-centered MLIPs lack physically motivated bonded/non-bonded interaction terms. Consequently, if local atomic environments underrepresented in the training dataset emerge during an MLIP-MD simulation, the prediction accuracy of atomic forces can significantly deteriorate, leading to unphysical trajectories and ultimately simulation collapse. This stability issue is particularly crucial for inhomogeneous systems such as defect-containing systems and amorphous systems, where large-scale, long-time MD simulations are essential to capture the inherent heterogeneity and slow dynamical processes

of the systems. Therefore, during the generation of training data for an MLIP model, it is imperative to sample diverse structures and construct a dataset that sufficiently encompasses the local atomic environments likely to emerge during production MD runs.

We have been developing a software package⁴⁷ for constructing a robust NNP applicable to large-scale, long-time MD simulations by generating a dataset encompassing diverse structures through active learning (AL).⁴⁸ Our NNP generator streamlines the complex steps involved in NNP construction, such as structure sampling, screening, labeling with electronic structure calculations, model training, and accuracy evaluation. Furthermore, by combining structure sampling via non-equilibrium NNP-MD simulations with screening in a structural feature space considering minimum interatomic distances, our NNP generator allows for efficient sampling of off-equilibrium structures, enhancing the robustness of the NNP for long-time simulations.⁴⁷

In this study, using our NNP generator, we construct an NNP model for polymer electrolyte membranes, Nafion, and perform long-time NNP-MD simulations of large Nafion systems ranging from approximately 10,000 to 20,000 atoms. Nafion membranes display diverse and highly heterogeneous morphologies that are dependent on the hydration level.⁴⁹ As such, large-scale, long-time MD simulations are crucial for accurately capturing proton transport in Nafion membranes. We perform MD simulations of large Nafion systems using the NNP model generated by our tool and evaluate the simulation stability based on the uncertainty in the predicted atomic forces. Accordingly, we augment the dataset and retrain the NNP to construct a robust NNP model suitable for large-scale, long-time MD simulations. Using the final NNP model, we successfully perform stable, large-scale NNP-MD simulations of Nafion systems for an extended duration of 31 ns. Moreover, the self-diffusion coefficients of hydrogen atoms obtained from our NNP-MD simulations show good agreement with experimental values over a wider range of hydration levels

compared to previous *ab initio* MD (AIMD)^{50,51} and MLIP-MD simulations.⁴⁰ We opine that this study presents a methodology for constructing a robust NNP that is essential for conducting large-scale, long-time NNP-MD simulations.

2. METHODS

This section describes the methods for constructing NNP models for Nafion systems in Section 2.1 and the conditions for long-time NNP-MD simulations of large Nafion systems in Section 2.2.

2.1. Construction of NNP models. The process of constructing an NNP model for simulating Nafion systems is illustrated in Figure 1. Each phase of this process is described in detail below.

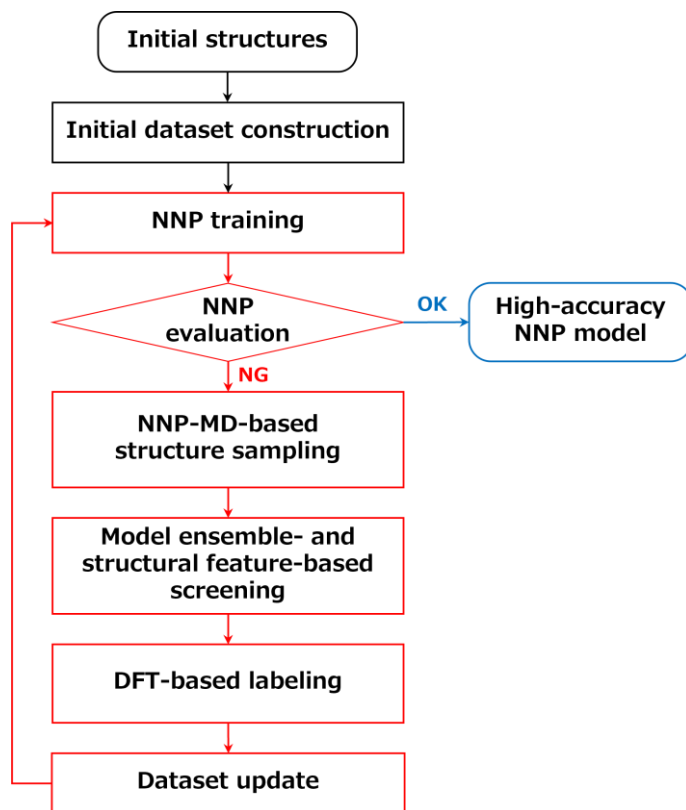


Figure 1. A flowchart of the NNP model construction process for Nafion systems.

2.1.1. Preparation of Initial Structures. Multiple systems comprising Nafion monomers and water molecules are used as the initial structures for NNP training. As shown in Figure 2(a), the Nafion monomer consists of a hydrophobic Teflon backbone composed of carbon and fluorine atoms and a perfluoro side chain with a sulfonic acid group, totaling 71 atoms. The initial structures are constructed with hydration levels $\lambda = 0, 1, 7,$ and 13 . These systems comprise four Nafion monomers ($\lambda = 0$), three monomers and 3 water molecule ($\lambda = 1$), three monomers and 21 water molecules ($\lambda = 7$), and two monomers and 26 water molecules ($\lambda = 13$), respectively (Figure 2(b)). Here, λ is defined as the number of H_2O molecules per SO_3^- group. Additionally, a system consisting of 32 water molecules is also included in the training structures. RadonPy⁵² is employed to generate the initial structures of the Nafion systems. Section S1 of the Supporting Information details the procedure for generating these initial structures.

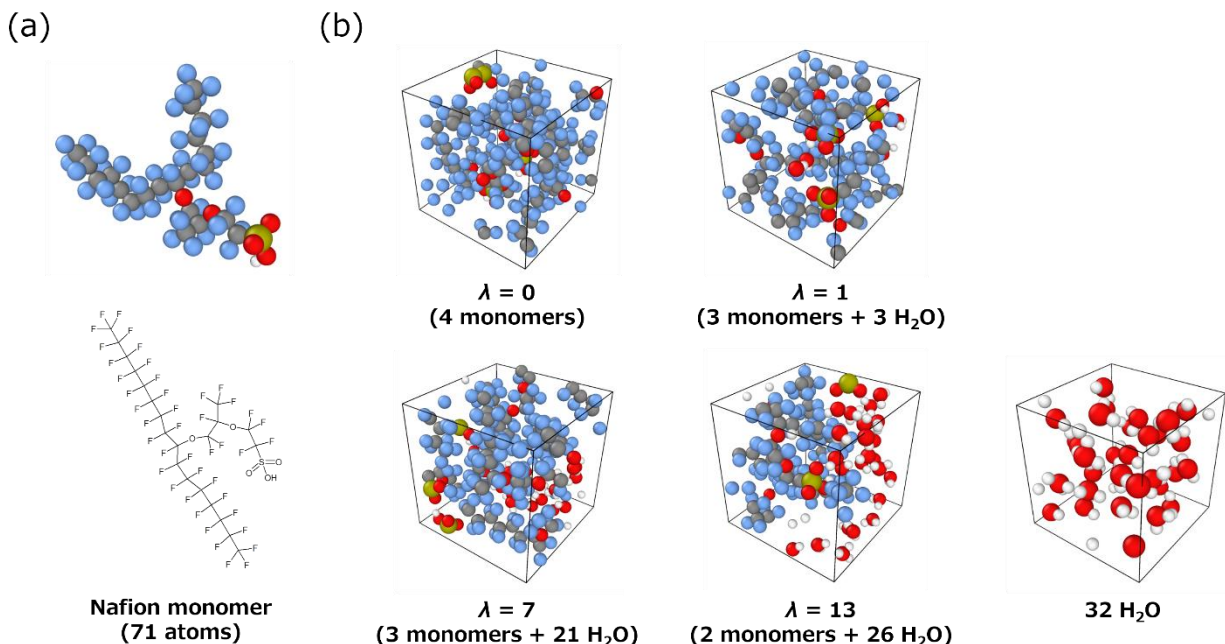


Figure 2. Nafion systems used for NNP training. (a) Monomer structure with 71 atoms. (b) Nafion systems and a water system. The hydration levels, λ , of the Nafion systems are 0 (4 monomers), 1 (3 monomers and 3 H₂O molecules), 7 (3 monomers and 21 H₂O molecules), and 13 (2 monomers and 26 H₂O molecules). The white, gray, red, blue, and yellow spheres represent hydrogen, carbon, oxygen, fluorine, and sulfur atoms, respectively. All the systems are visualized using OVITO.⁵³

2.1.2. Active Learning of NNPs. As described in our previous work,⁴⁷ a single active-learning (AL) loop comprises the following steps: NNP-MD-based structure sampling, model ensemble- and structural feature-based two-stage screening, DFT-based labeling, and retraining of the NNPs with the augmented dataset. Increasing the number of AL-loop iterations enhances the structural diversity within the dataset. In this study, a total of 17 AL loops are performed, as outlined in Table 1. Furthermore, to construct the initial NNPs for the first AL loop (iteration 1), an initial dataset is

generated from *ab initio* MD (AIMD) simulations and used for training the initial NNPs (iteration 0). The details of each phase are described below.

Table 1. The Sampling Method Used in Each AL Loop and the Numbers of Sampled, Screened, and DFT-Labeled Structures

Iter.	Sampling				1st Screening	2nd Screening	Labeling
	Method	Conditions ^a	Length (ps)	# of structures	# of structures	# of structures	# of structures
0	AIMD	NVT ($T = 400$ K for Nafion, 353 K for water)	1	1,000	—	—	1,000
1	DPMD	NVT, NPT ($T = 300, 600, 900$ K)	50	13,707	2,043	1,000	784
2	DPMD	NVT, NPT ($T = 300, 600, 900$ K)	50	22,018	10,293	1,000	944
3	DPMD	NVT, NPT ($T = 300, 600, 900$ K)	50	23,727	9,808	1,000	995
4	DPMD	NVT, NPT ($T = 300$ – 700 K ^b)	100	37,593	16,128	1,000	982
5	DPMD	NVT, NPT ($T = 300$ – 700 K ^b)	100	39,870	18,659	1,000	979
6	DPMD	NVT, NPT ($T = 300$ – 700 K ^b)	100	35,701	15,776	1,000	998
7	DPMD	NVT, NPT ($T = 300$ – 700 K ^b)	100	42,076	25,873	1,000	981

8	DPMD	NVT, NPT ($T = 300\text{--}700\text{ K}^b$)	100	42,818	23,929	1,000	944
9	DPMD	NVT, NPT ($T = 300\text{--}700\text{ K}^b$)	100	43,812	29,374	1,000	929
10	DPMD	NVT, NPT ($T = 300\text{--}700\text{ K}^b$)	100	42,204	23,289	1,000	886
11	NE- DPMD	Volume contraction ($\times 0.7$, $T = 300\text{--}700\text{ K}^b$)	10	50,000	31,844	1,000	993
12	NE- DPMD	Volume contraction ($\times 0.7$, $T = 300\text{--}700\text{ K}^b$)	10	50,000	31,379	1,000	876
13	NE- DPMD	Volume contraction ($\times 0.7$, $T = 300\text{--}700\text{ K}^b$)	10	50,000	36,827	1,000	893
14	NE- DPMD	Volume contraction ($\times 0.7$, $T = 300\text{--}700\text{ K}^b$)	10	48,713	30,584	1,000	980
15	NE- DPMD	Volume contraction ($\times 0.7$, $T = 300\text{--}700\text{ K}^b$)	10	50,000	36,918	1,000	998
16	NE- DPMD	Volume contraction ($\times 0.7$, $T = 300\text{--}700\text{ K}^b$)	10	50,000	37,919	1,000	1,000
17	NE- DPMD	Volume expansion ($\times 2$, $T = 300\text{--}700\text{ K}^b$)	10	50,000	32,510	1,000	603

^aThe pressures during DPMD sampling in the NPT ensemble are set to be 1 bar. ^bThe temperature interval is 100 K.

Construction of the Initial Dataset. To generate the initial dataset for training the initial NNPs, AIMD simulations are performed for each system shown in Figure 2(b) using Quantum ESPRESSO.^{54,55} The revPBE functional^{56,57} is employed with Grimme’s D3 dispersion correction.⁵⁸ The pseudopotentials of the projector augmented wave (PAW) form⁵⁹ are used. The kinetic energy cutoffs for wavefunctions and charge density are set to 70 Ry and 280 Ry, respectively. The Γ point is used for the Nafion systems, while a four k-point mesh is used for the water system. The timestep size is set to 0.5 fs. All AIMD simulations are performed in the NVT ensemble for 1 ps under the periodic boundary conditions. The temperatures of the Nafion systems and the water system are maintained at 400 K and 353 K, respectively, using the Berendsen thermostat⁶⁰ with a time constant of 50 fs. Frames are stored every 50 fs, resulting in 200 frames per system, totaling 1,000 frames. The frames for each system are randomly divided into training and validation datasets with an 8:2 ratio. Each frame contains labels for total energy and atomic forces.

NNP Training. DeePMD-kit 2.2.4⁶¹ is used for NNP training. The se_e2_a descriptor of DeepPot-SE¹¹ is employed with a cutoff radius of 6 Å. The embedding and fitting networks consist of (25, 50, 100) and (120, 120, 120) nodes with ResNet-like architectures,⁶² respectively. The number of training steps is set to 500,000 in iterations 0–16 and 2,000,000 in iteration 17. The batch size is 1. The learning rate decays exponentially from 1.0×10^{-3} to 1.0×10^{-8} with 5,000 decay steps. The training labels are total energy and atomic forces. The loss function is a weighted sum of energy and force loss terms, where the prefactor for each term varies linearly with respect to the learning rate. The prefactors for the energy and force loss terms at the initial training step are set to 0.02 and 1,000, respectively, and both converge to 1 as the number of training steps approaches infinity. The Adam stochastic gradient descent method⁶³ is used to train four Deep Potential (DP) models

with independently initialized weight parameters. These four DP models are used to calculate the model deviations of atomic forces⁶⁴ in the screening phase.

Sampling. To sample candidate structures to be added to the dataset, multiple DPMD simulations are performed for each system shown in Figure 2(b) using one of the four DP models generated in the previous AL loop. The conditions for the DPMD simulations in each AL loop are summarized in Table 1. In AL-loop iterations 1–10, DPMD sampling is performed in the NVT and NPT ensembles with varied temperatures, where the target pressure in the NPT ensemble is set to 1 bar. In iterations 11–16, non-equilibrium DPMD (NE-DPMD) sampling is performed by compressing the simulation cell volumes to 70% of their original size ($\times 0.7$). Subsequently, in iteration 17, NE-DPMD sampling is conducted by expanding the simulation cell volumes to twice their original size ($\times 2$). As discussed in Section 3.1, the NE-DPMD sampling from iteration 11 onwards aims to improve the stability of DPMD simulations by introducing off-equilibrium structures into the dataset. Specifically, the compression simulations in iterations 11–16 aim to sample structures with short interatomic distances, while the expansion simulation in iteration 17 focuses on sampling intermolecular interactions, which significantly affect the thermodynamic properties of a reference system.⁴⁶ The timestep size is set to 0.5 fs and the temperature and pressure are controlled using the Nosé–Hoover style thermostat^{65,66} and barostat,^{67,68} respectively. Frames are extracted from each DPMD simulation at intervals of 50 fs in AL-loop iterations 1–3, 100 fs in iterations 4–10, and 5 fs in iterations 11 and later. However, if a DPMD simulation collapses prematurely, frames are extracted only up to the point of simulation collapse. LAMMPS⁶⁹ is used to perform the DPMD simulations. Table 1 lists the number of structures sampled in each AL loop. In the initial AL-loop iterations, the accuracy of the DP model is low, leading to premature collapse in DPMD simulations and consequently fewer sampled structures. As the AL loop progresses and the DP

model accuracy improves, more DPMD simulations complete successfully, resulting in an increased number of sampled structures.

Screening. The structures obtained in the sampling phase undergo a two-stage screening process. The first stage involves screening based on the model deviation of predicted atomic forces.⁶⁴ Atomic forces are predicted for each structure using the four DP models, and the maximum standard deviation of these predictions is calculated. Only structures with maximum standard deviations within a specific range are selected. In this study, the lower and upper thresholds are set to 0.05 eV/Å and 0.2 eV/Å, respectively. This allows for the exclusion of structures already well-represented in the current dataset and those with very high uncertainty, which are likely to be unphysical, enabling efficient and incremental improvement of the NNP accuracy. Following the first screening, candidate structures undergo a second screening based on structural features.⁷⁰ As shown in Table 1, the number of structures selected in the first stage ranges from at least 2,000 to over 30,000 in some cases. Performing DFT calculations for all these structures is computationally prohibitive. Moreover, the selected structures often include many similar configurations in terms of structural features, resulting in redundant structural data. Consequently, the objective of the second screening is to achieve a more uniform selection of structurally diverse candidates by eliminating those exhibiting high proximity within the structural feature space. Here, the atom-wise outputs of the DP model’s embedding network are concatenated and dimensionally reduced to a 2D feature space using densMAP.⁷¹ Subsequently, screening is performed based on inter-point distances within this feature space, aiming to sample data points that are maximally distant from existing data points and ensure that the selected data points are also well-separated from each other. In AL-loop iterations 1–10 and 17, screening is performed in this 2D structural feature space. In iterations 11–16, screening is performed in a 3D structural feature space, incorporating an

additional feature related to the minimum interatomic distance.⁴⁷ As discussed in Section 3.1, the minimum O–H distance is used as the third dimension in iterations 11–13, and the minimum F–S distance is used in iterations 14–16. For more details regarding the screening in the 3D structural feature space, please refer to our previous work.⁴⁷ Table 1 shows the number of structures selected after the model ensemble-based and structural feature-based screening. In this study, 1,000 structures are selected after the structural feature-based screening.

Labeling. DFT calculations are performed for the 1,000 structures selected in the screening phase to obtain labels for total energy and atomic forces. The DFT calculation conditions are identical to those used for generating the initial dataset. For each system, the newly labeled frames are randomly divided into training and validation datasets with an 8:2 ratio. However, structures with a maximum atomic force greater than 20 eV/Å are excluded from the dataset. Table 1 shows the final number of structures labeled by DFT calculations. The discrepancy between the number of structures after screening (1,000) and that of labeled structures arises from the exclusion of structures for which DFT calculations did not converge or those exhibiting maximum atomic forces greater than 20 eV/Å.

The energy and force root-mean-square errors (RMSEs) at the end of AL loop iterations 10, 13, 16, and 17 are presented in Table 2. In all the iterations, the energy RMSEs on the validation set are at most around 2 meV/atom, indicating high accuracy in energy prediction. The force RMSEs are consistently larger for the Nafion systems compared to the pure water system in all iterations. This is attributed to the greater diversity of atomic environments in the five-element hydrated Nafion systems compared to the two-element water system, making the prediction of

atomic forces more challenging. Nevertheless, at the end of iteration 17 with the training steps increased to 2,000,000, the force RMSEs for the Nafion systems are at most approximately 65 meV/Å, and the force RMSE for the pure water system is below 50 meV/Å. These results demonstrate sufficiently high accuracy in predicting atomic forces for multiple systems using a single DP model.

Table 2. Energy and Force RMSEs in Iteration 10, 13, 16, and 17^a

Iter.	System	Training		Validation	
		Energy (meV/atom)	Force (meV/Å)	Energy (meV/atom)	Force (meV/Å)
10	Nafion ($\lambda = 0$)	0.76	75.5	0.79	75.3
	Nafion ($\lambda = 1$)	1.39	80.3	1.77	81.2
	Nafion ($\lambda = 7$)	0.78	78.0	1.24	79.2
	Nafion ($\lambda = 13$)	1.25	75.3	0.93	74.6
	Water	1.32	52.9	1.31	53.9
13	Nafion ($\lambda = 0$)	1.09	79.0	1.42	79.2
	Nafion ($\lambda = 1$)	1.67	81.7	1.66	82.7
	Nafion ($\lambda = 7$)	0.97	79.5	1.58	80.7
	Nafion ($\lambda = 13$)	1.26	77.3	0.94	76.3
	Water	1.34	60.7	1.33	62.2
16	Nafion ($\lambda = 0$)	1.02	85.0	1.28	85.6
	Nafion ($\lambda = 1$)	1.51	85.2	1.45	86.1
	Nafion ($\lambda = 7$)	0.93	82.5	1.42	83.2
	Nafion ($\lambda = 13$)	1.34	82.1	0.96	81.2
	Water	1.28	59.6	1.22	60.4
17	Nafion ($\lambda = 0$)	0.73	62.5	0.92	63.3
	Nafion ($\lambda = 1$)	1.02	63.5	1.02	64.6
	Nafion ($\lambda = 7$)	0.70	64.0	1.02	64.8
	Nafion ($\lambda = 13$)	0.92	63.6	0.69	63.2
	Water	1.05	47.4	1.01	48.2

^aThe training and validation data are split at an 8:2 ratio in each iteration. The training steps are set to 2,000,000 in iteration 17, whereas they are set to 500,000 in all other iterations.

2.2. Large-Scale NNP-MD Simulations. Long-time MD simulations of large Nafion systems are performed using the trained DP models. Ten Nafion oligomers with a degree of polymerization of 14 (Figure 3(a)) are placed in the simulation box, along with water molecules to create the Nafion systems with $\lambda = 0, 3, 6, 12, 18,$ and 24 (Figure 3(b)). The systems with $\lambda = 0, 3, 6, 12, 18,$ and 24 contain 9680, 10940, 12200, 14720, 17240, and 19760 atoms, respectively. To assess the structure dependence of physicochemical properties, three independent systems are generated for each hydration level. RadonPy⁵² is employed to create these initial structures. Section S1 of the Supporting Information details the procedure for generating these initial structures.

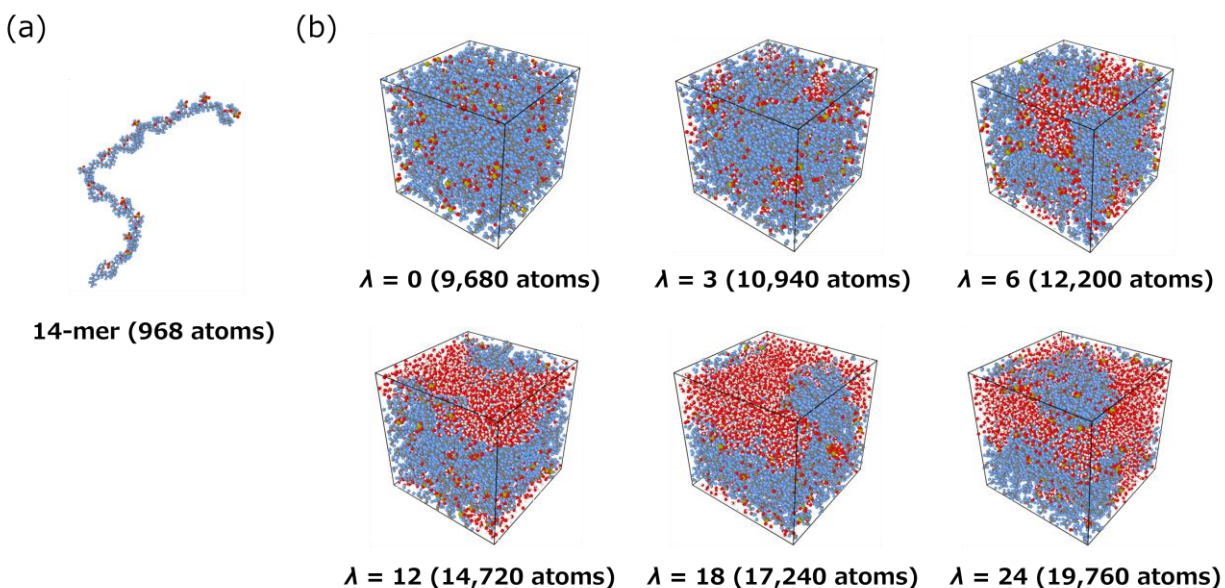


Figure 3. Nafion systems used for large-scale NNP-MD simulations. (a) Nafion 14-mer structure with 968 atoms. (b) Nafion systems with $\lambda = 0$ (9,680 atoms), 3 (10,940 atoms), 6 (12,200 atoms), 12 (14,720 atoms), 18 (17,240 atoms), and 24 (19,760 atoms). The number of 14-mers in each system is 10, while the number of water molecules is 0, 420, 840, 1,680, 2,520, and 3,360 for $\lambda = 0, 3, 6, 12, 18,$ and 24 , respectively.

Using the generated initial structures, DPMD simulations are performed in the NPT ensemble at a temperature of 298 K and a pressure of 1 bar. The timestep size is set to 0.5 fs and the maximum simulation time is 31 ns. The temperature and pressure are controlled using the Nosé–Hoover style thermostat^{65,66} and barostat^{67,68} with the time constants of 50 fs and 500 fs, respectively. To evaluate the model deviations of the atomic forces at each timestep, forces acting on atoms in the system are predicted using the four NNPs and the standard deviation of these predictions is calculated.

3. RESULTS AND DISCUSSION

In this section, we discuss the stability of the NNP-MD simulations using DP models constructed in different iterations in Section 3.1. Here, we find that the DP model constructed in iteration 17 enables large-scale (10,000–20,000 atoms), long-time (>30 ns) NNP-MD simulations for all the Nafion systems shown in Figure 3(b). Section 3.2 presents equilibrium densities of the Nafion systems and self-diffusion coefficients of hydrogen atoms calculated from the NNP-MD simulations using the DP model constructed in iteration 17. Hereafter, the DP model constructed in iteration x will be referred to as DP-iter- x .

3.1. Stability of DPMD Simulations. Figure 4 summarizes the stability of MD simulations of the Nafion system with $\lambda = 3$ using DP-iter-10, -13, -16, and -17 models. The MD simulation using the DP-iter-10 model exhibits a sudden decrease in the density and potential energy around 0.41 ns, indicating simulation collapse. Correspondingly, the maximum model deviation of atomic forces also increases sharply around 0.41 ns. Although the apparent simulation collapse occurs around 0.41 ns, the maximum model deviation of atomic forces exceeds 1 eV/Å much earlier,

around 0.134 ns, suggesting instability in the MD simulation. Therefore, to ensure the stability of long-time DPMD simulations, it is essential to suppress such abrupt increases in the maximum model deviation of atomic forces.

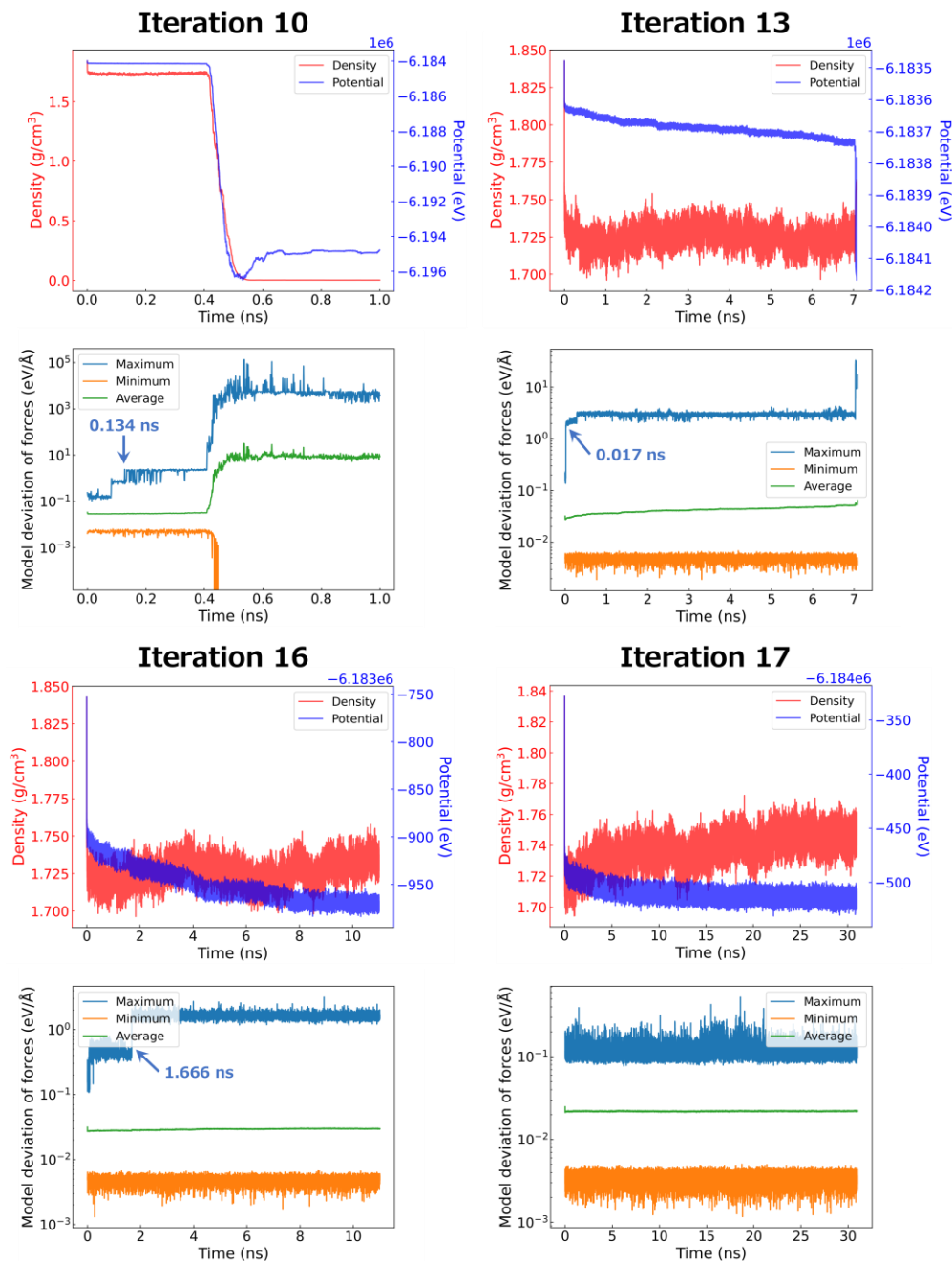


Figure 4. Temporal changes in the densities, potential energies, and model deviations of forces for the Nafion system with $\lambda = 3$ simulated using the DP-iter-10, -13, -16, and -17 models. The model deviations of forces are calculated for all the atoms and their maximum, minimum, and average values are presented. The arrows in the bottom figures indicate the times when the maximum model deviations of forces exceed 1 eV/Å (see Figure 5).

Figure 5(a) compares the magnitudes and model deviations of atomic forces for the MD snapshot at $t = 0.134$ ns using the DP-iter-10 models. As described in Section 2.2, the model deviations of the atomic forces are calculated from the predictions by the four DP-iter-10 models. The atoms exhibiting model deviations exceeding 1 eV/\AA are H and O atoms. We find that the large model deviations for the H and O atoms are attributed to short O–H distances emerging in the MD simulation, of which atomic environments are underrepresented in the training dataset. To address this issue, as shown in Table 1, iterations 11–13 employ structure sampling during volume compression using NE-DPMD simulations to capture off-equilibrium structures with short interatomic distances. Furthermore, the second screening stage based on structural features incorporates the minimum O–H distance as an additional feature in a 3D structural feature space. This combination of NE-DPMD sampling with the 3D structural feature-based screening enables more efficient selection of off-equilibrium structures with short O–H distances.⁴⁷

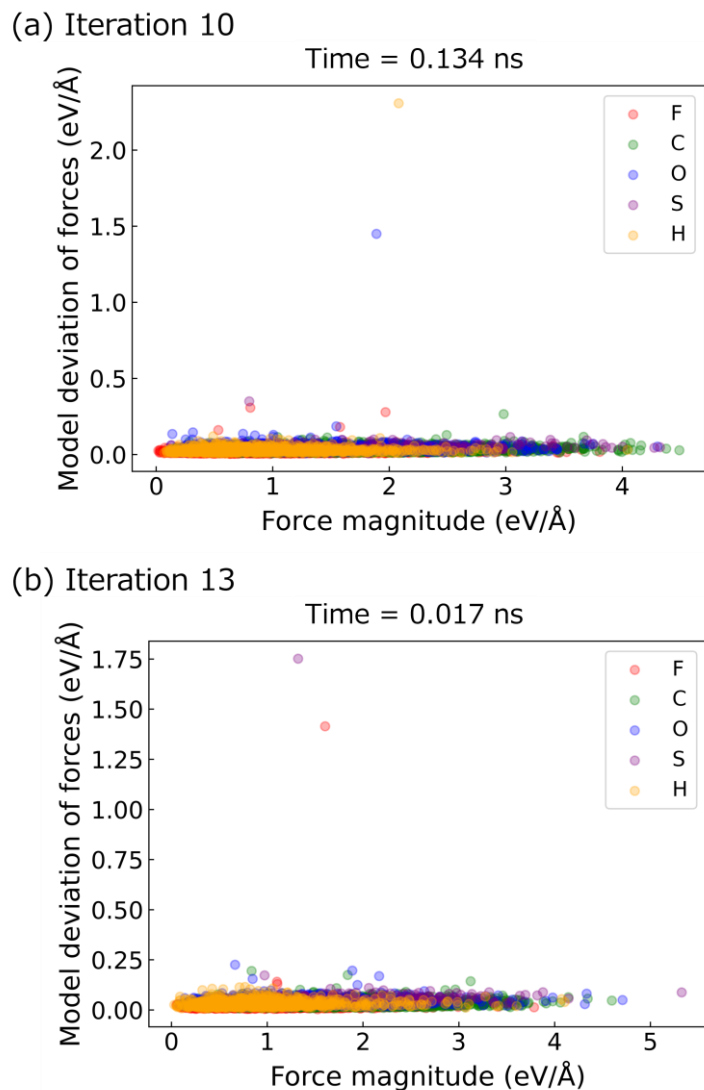


Figure 5. Comparison of the magnitudes and model deviations of atomic forces for the MD snapshot at $t = 0.134$ ns using the DP-iter-10 models (a) and the MD snapshot at $t = 0.017$ ns using the DP-iter-13 models (b).

As shown in Figure 4, the MD simulation using the DP-iter-13 model seems to be stable in terms of the density and potential energy up to around 7 ns. Subsequently, the potential energy decreases abruptly, coinciding with a sharp increase in the maximum model deviation of atomic

forces, leading to simulation collapse. However, the maximum model deviation of atomic forces surpasses 1 eV/Å much earlier, around 0.017 ns, indicating underlying instability in the MD simulation. As shown in Figure 5(b), model deviations exceeding 1 eV/Å are observed for F and S atoms due to underrepresented short F–S distances in the training dataset. To address this, iterations 14–16 employ NE-DPMD simulations with volume compression for structure sampling. The minimum F–S distance is then incorporated as an additional feature in the second screening stage, enabling targeted selection of off-equilibrium structures with short F–S distances.

As shown in Figure 4, the MD simulation using the DP-iter-16 model seems stable in terms of the density and potential energy for over 10 ns. Although the maximum model deviation of atomic forces exceeds 1 eV/Å earlier, around 1.666 ns, the stability of the MD simulation is significantly improved compared to the simulations using the DP-iter-10 and -13 models. We find that the increase in the maximum model deviation of atomic forces is due to protons erroneously approaching the ether oxygen atoms of the Nafion oligomers in the MD simulation using the DP-iter-16 model. The structures including such atomic environments are not present in the dataset because it is almost impossible to converge DFT calculations of such unphysical structures. To address this issue, the Ziegler–Biersack–Littmark (ZBL) repulsive potential,⁷² with inner and outer cutoffs of 0.1 Å and 2 Å, respectively, is introduced between hydrogen atoms and the ether oxygen atoms of the Nafion oligomer. Furthermore, in iteration 17, structure sampling is performed during volume expansion using NE-DPMD simulations to sample a wider range of intermolecular interactions, (Table 1).

As shown in Figure 4, the MD simulation using the DP-iter-17 model remains stable for an extended duration of 31 ns. Furthermore, the maximum model deviation of atomic forces remains on the order of 10^{-1} eV/Å, indicating the stability of the MD simulation. As shown in Figure S1 of

the Supporting Information, the MD simulations for all other hydration levels also remain stable for durations of 31 ns. These results demonstrate the successful construction of an NNP capable of performing large-scale, long-time MD simulations. The following discussion focuses on the results obtained from MD simulations using the DP-iter-17 model.

3.2. Physical Properties. Figure 6 compares the densities of the Nafion systems obtained from our DPMD simulations with the experimental values.⁷³ Although the densities from the DPMD simulations are slightly lower than the experimental values, the qualitative trend of hydration level dependence is accurately reproduced. Notably, the small standard deviations observed across three independent systems at each hydration level demonstrate that our large-scale, long-time DPMD simulations effectively minimize statistical uncertainty in the calculated densities, providing robust and reliable results. We hypothesize that the underestimation of densities can be, at least in part, attributed to the choice of the revPBE functional^{56,57} employed for the DFT-based labeling. This inference is supported by prior research; for example, a previous study³⁵ reported a similar underestimation of water density (approximately 10%) when using NNP models trained on DFT data generated with the RPBE functional⁷⁴ and Grimme’s D3 dispersion correction.⁵⁸

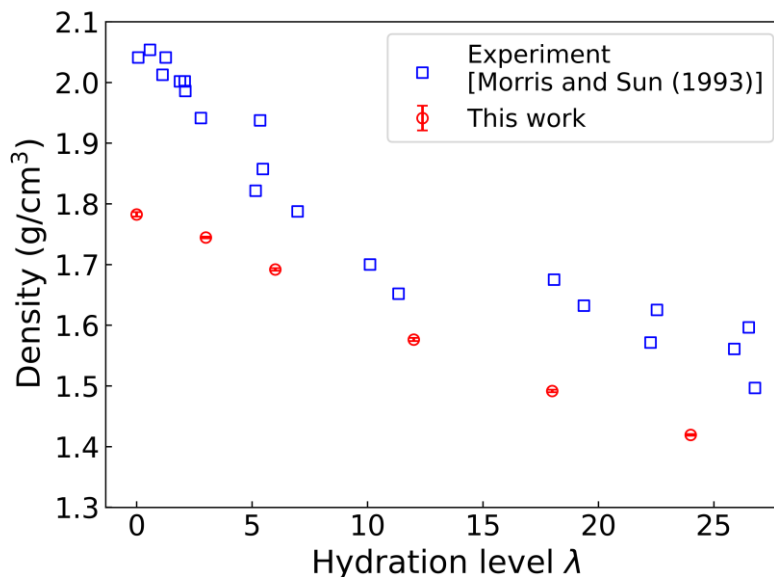


Figure 6. Comparison of the MD-calculated densities of the hydrated Nafion systems with the experimental counterparts.⁷³ The error bars of the calculated densities are the standard deviations obtained from three independent simulations starting from different structures.

The mean-squared displacements (MSDs) of hydrogen atoms in the hydrated Nafion systems are shown in Figure 7(a). Each MSD is calculated over a 5-ns period using the trajectory from 21 ns to 31 ns, where the time origin is shifted by 0.2-ns increments to improve statistical sampling. The diffusivity of hydrogen atoms clearly increases with increasing hydration level. The large-scale, long-time DPMD simulations effectively reduce the standard deviations of the MSDs and capture the diffusive regime where the MSD is proportional to time. Figure 7(b) shows the self-diffusion coefficients of hydrogen atoms, calculated from the slopes of the MSDs in the range of 3–5 ns at each hydration level using the Einstein’s relationship.⁷⁵ Our DPMD simulations yield the self-diffusion coefficients of hydrogen atoms that closely match experimental values^{76,77} in a

wide range of hydration levels. In contrast, previous AIMD simulations fail to quantitatively reproduce the self-diffusion coefficients due to the limitations in system size and simulation time.^{50,51} While MD simulations using a Gaussian approximation potential (GAP)⁴⁰ reproduce the self-diffusion coefficients for $\lambda = 3$ and 6, they underestimate the self-diffusion coefficient for $\lambda = 12$. This result suggests that the limited system size (approximately 1,000 atoms) and short simulation time (approximately 200 ps) employed in the GAP-MD simulations are insufficient to adequately capture the transport properties of hydrogen atoms in highly heterogeneous hydrated Nafion systems at higher hydration levels. In contrast, our DPMD simulations, performed for 31 ns on the hydrated Nafion systems with over 10,000 atoms, accurately reproduce the transport properties of hydrogen atoms. Remarkably, our DPMD simulations accurately reproduce the self-diffusion coefficients even for hydration levels up to 24 in the production runs, despite the training systems only including hydration levels up to 13 (Figure 2(b)). This successful extrapolation beyond the training domain is attributed to the diversity of local atomic environments captured within the training dataset. Specifically, the active-learning procedure enables the sampling of a wide range of structural configurations, resulting in a dataset rich in diverse atomic environments. Consequently, the DP model developed in this study accurately reproduces the transport properties of hydrogen atoms even in the systems outside the training domain in terms of the hydration level, owing to the comprehensive representation of local atomic environments achieved through active learning.

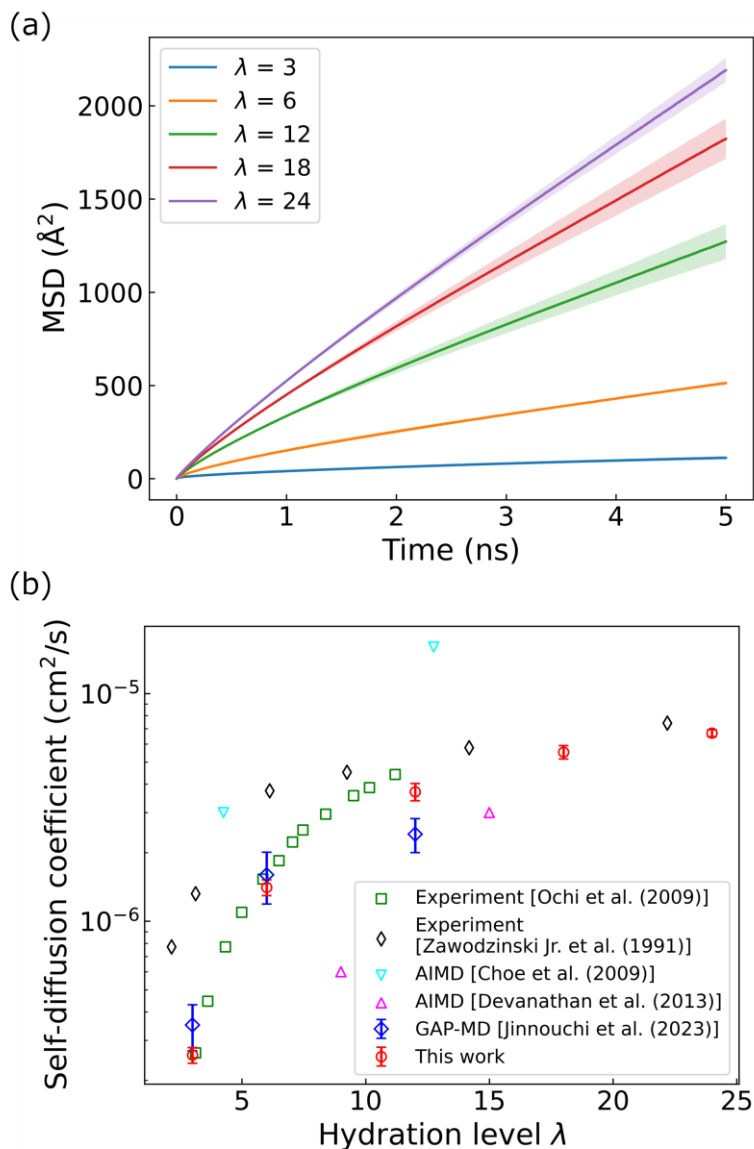


Figure 7. (a) The MSDs of hydrogen atoms in the hydrated Nafion systems with $\lambda = 3, 6, 12, 18$, and 24. The shaded areas represent the standard deviations obtained from three independent simulations starting from different structures. (b) Comparison of the calculated self-diffusion coefficients of hydrogen atoms in the hydrated Nafion systems with the experimental,^{76,77} AIMD-calculated,^{50,51} and GAP-MD-calculated⁴⁰ values. The error bars of the calculated self-diffusion coefficients are the standard deviations obtained from three independent simulations starting from different structures.

4. CONCLUSIONS

This study presents a neural network potential (NNP) model, constructed using our NNP generator, that enables large-scale, long-time molecular dynamics (MD) simulations of perfluorinated ionomer membranes (Nafion) across a wide range of hydration levels. A robust deep potential (DP) model is successfully built through iterative dataset expansion using active-learning loops. Specifically, the DP model’s robustness is significantly enhanced by combining non-equilibrium DPMD simulations, used to sample off-equilibrium structures, with structure screening in a 3D structural feature space incorporating minimum interatomic distances. This approach allows for stable MD simulations of large Nafion systems ranging from approximately 10,000 to 20,000 atoms for an extended duration of 31 ns. The MD simulations using the developed DP model yield the diffusion coefficients of hydrogen atoms that more closely match experimental values compared to previous *ab initio* MD and Gaussian approximation potential-based MD simulations. We opine that this active-learning strategy for constructing robust NNPs is applicable to a wide range of materials and represents a crucial technique for enabling stable, large-scale, long-time NNP-MD simulations.

REFERENCES

- (1) Noé, F.; Tkatchenko, A.; Müller, K. R.; Clementi, C. Machine Learning for Molecular Simulation. *Annu. Rev. Phys. Chem.* **2020**, *71*, 361–390. <https://doi.org/10.1146/annurev-physchem-042018-052331>.
- (2) Unke, O. T.; Chmiela, S.; Sauceda, H. E.; Gastegger, M.; Poltavsky, I.; Schütt, K. T.; Tkatchenko, A.; Müller, K.-R. Machine Learning Force Fields. *Chem. Rev.* **2021**, *121* (16), 10142–10186. <https://doi.org/10.1021/acs.chemrev.0c01111>.
- (3) Kocer, E.; Ko, T. W.; Behler, J. Neural Network Potentials: A Concise Overview of Methods. *Annu. Rev. Phys. Chem.* **2022**, *73*, 163–186. <https://doi.org/10.1146/annurev-physchem-082720-034254>.

- (4) Bartók, A. P.; Payne, M. C.; Kondor, R.; Csányi, G. Gaussian Approximation Potentials: The Accuracy of Quantum Mechanics, without the Electrons. *Phys. Rev. Lett.* **2010**, *104* (13), 136403. <https://doi.org/10.1103/PhysRevLett.104.136403>.
- (5) Bartók, A. P.; Kondor, R.; Csányi, G. On Representing Chemical Environments. *Phys. Rev. B* **2013**, *87* (18), 184115. <https://doi.org/10.1103/PhysRevB.87.184115>.
- (6) Thompson, A. P.; Swiler, L. P.; Trott, C. R.; Foiles, S. M.; Tucker, G. J. Spectral Neighbor Analysis Method for Automated Generation of Quantum-Accurate Interatomic Potentials. *J. Comput. Phys.* **2015**, *285*, 316–330. <https://doi.org/10.1016/j.jcp.2014.12.018>.
- (7) Chmiela, S.; Sauceda, H. E.; Müller, K.-R.; Tkatchenko, A. Towards Exact Molecular Dynamics Simulations with Machine-Learned Force Fields. *Nat. Commun.* **2018**, *9*, 3887. <https://doi.org/10.1038/s41467-018-06169-2>.
- (8) Behler, J. Four Generations of High-Dimensional Neural Network Potentials. *Chem. Rev.* **2021**, *121* (16), 10037–10072. <https://doi.org/10.1021/acs.chemrev.0c00868>.
- (9) Smith, J. S.; Isayev, O.; Roitberg, A. E. ANI-1: An Extensible Neural Network Potential with DFT Accuracy at Force Field Computational Cost. *Chem. Sci.* **2017**, *8* (4), 3192–3203. <https://doi.org/10.1039/C6SC05720A>.
- (10) Gastegger, M.; Schwiedrzik, L.; Bittermann, M.; Berzsenyi, F.; Marquetand, P. wACSF—Weighted Atom-Centered Symmetry Functions as Descriptors in Machine Learning Potentials. *J. Chem. Phys.* **2018**, *148* (24), 241709. <https://doi.org/10.1063/1.5019667>.
- (11) Zhang, L.; Han, J.; Wang, H.; Saidi, W.; Car, R.; E, W. End-to-End Symmetry Preserving Inter-Atomic Potential Energy Model for Finite and Extended Systems. In *Advances in Neural Information Processing Systems*; Curran Associates, Inc., 2018; Vol. 31.
- (12) Yao, K.; Herr, J. E.; Toth, D. W.; Mckintyre, R.; Parkhill, J. The TensorMol-0.1 Model Chemistry: A Neural Network Augmented with Long-Range Physics. *Chem. Sci.* **2018**, *9* (8), 2261–2269. <https://doi.org/10.1039/C7SC04934J>.
- (13) Zhang, Y.; Hu, C.; Jiang, B. Embedded Atom Neural Network Potentials: Efficient and Accurate Machine Learning with a Physically Inspired Representation. *J. Phys. Chem. Lett.* **2019**, *10* (17), 4962–4967. <https://doi.org/10.1021/acs.jpcclett.9b02037>.
- (14) Schütt, K. T.; Sauceda, H. E.; Kindermans, P.-J.; Tkatchenko, A.; Müller, K.-R. SchNet – A Deep Learning Architecture for Molecules and Materials. *J. Chem. Phys.* **2018**, *148* (24), 241722. <https://doi.org/10.1063/1.5019779>.
- (15) Unke, O. T.; Meuwly, M. PhysNet: A Neural Network for Predicting Energies, Forces, Dipole Moments, and Partial Charges. *J. Chem. Theory Comput.* **2019**, *15* (6), 3678–3693. <https://doi.org/10.1021/acs.jctc.9b00181>.
- (16) Zubatyuk, R.; Smith, J. S.; Leszczynski, J.; Isayev, O. Accurate and Transferable Multitask Prediction of Chemical Properties with an Atoms-in-Molecules Neural Network. *Sci. Adv.* **2019**, *5* (8), eaav6490. <https://doi.org/10.1126/sciadv.aav6490>.
- (17) Schütt, K.; Unke, O.; Gastegger, M. Equivariant Message Passing for the Prediction of Tensorial Properties and Molecular Spectra. In *Proceedings of the 38th International Conference on Machine Learning*; PMLR, 2021; pp 9377–9388.
- (18) Unke, O. T.; Chmiela, S.; Gastegger, M.; Schütt, K. T.; Sauceda, H. E.; Müller, K. R. SpookyNet: Learning Force Fields with Electronic Degrees of Freedom and Nonlocal Effects. *Nat. Commun.* **2021**, *12*, 7273. <https://doi.org/10.1038/s41467-021-27504-0>.
- (19) Gasteiger, J.; Groß, J.; Günnemann, S. Directional Message Passing for Molecular Graphs. arXiv April 5, 2022. <https://doi.org/10.48550/arXiv.2003.03123>.

- (20) Gasteiger, J.; Becker, F.; Günnemann, S. GemNet: Universal Directional Graph Neural Networks for Molecules. arXiv June 22, 2024. <https://doi.org/10.48550/arXiv.2106.08903>.
- (21) Batzner, S.; Musaelian, A.; Sun, L.; Geiger, M.; Mailoa, J. P.; Kornbluth, M.; Molinari, N.; Smidt, T. E.; Kozinsky, B. E(3)-Equivariant Graph Neural Networks for Data-Efficient and Accurate Interatomic Potentials. *Nat. Commun.* **2022**, *13*, 2453. <https://doi.org/10.1038/s41467-022-29939-5>.
- (22) Musaelian, A.; Batzner, S.; Johansson, A.; Sun, L.; Owen, C. J.; Kornbluth, M.; Kozinsky, B. Learning Local Equivariant Representations for Large-Scale Atomistic Dynamics. *Nat. Commun.* **2023**, *14*, 579. <https://doi.org/10.1038/s41467-023-36329-y>.
- (23) Thölke, P.; Fabritiis, G. D. TorchMD-NET: Equivariant Transformers for Neural Network Based Molecular Potentials. arXiv April 23, 2022. <https://doi.org/10.48550/arXiv.2202.02541>.
- (24) Liao, Y.-L.; Wood, B.; Das, A.; Smidt, T. EquiformerV2: Improved Equivariant Transformer for Scaling to Higher-Degree Representations. arXiv March 6, 2024. <https://doi.org/10.48550/arXiv.2306.12059>.
- (25) Frank, J. T.; Unke, O. T.; Müller, K.-R.; Chmiela, S. A Euclidean Transformer for Fast and Stable Machine Learned Force Fields. *Nat. Commun.* **2024**, *15*, 6539. <https://doi.org/10.1038/s41467-024-50620-6>.
- (26) Deringer, V. L.; Csányi, G. Machine Learning Based Interatomic Potential for Amorphous Carbon. *Phys. Rev. B* **2017**, *95* (9), 094203. <https://doi.org/10.1103/PhysRevB.95.094203>.
- (27) Sivaraman, G.; Krishnamoorthy, A. N.; Baur, M.; Holm, C.; Stan, M.; Csányi, G.; Benmore, C.; Vázquez-Mayagoitia, Á. Machine-Learned Interatomic Potentials by Active Learning: Amorphous and Liquid Hafnium Dioxide. *npj Comput. Mater.* **2020**, *6* (1), 1–8. <https://doi.org/10.1038/s41524-020-00367-7>.
- (28) Liu, Y.-B.; Yang, J.-Y.; Xin, G.-M.; Liu, L.-H.; Csányi, G.; Cao, B.-Y. Machine Learning Interatomic Potential Developed for Molecular Simulations on Thermal Properties of β -Ga₂O₃. *J. Chem. Phys.* **2020**, *153* (14), 144501. <https://doi.org/10.1063/5.0027643>.
- (29) Chen, D.; Shang, C.; Liu, Z.-P. Machine-Learning Atomic Simulation for Heterogeneous Catalysis. *npj Comput. Mater.* **2023**, *9* (1), 1–9. <https://doi.org/10.1038/s41524-022-00959-5>.
- (30) Liu, D.; Wu, Y.; Samatov, M. R.; Vasenko, A. S.; Chulkov, E. V.; Prezhdo, O. V. Compression Eliminates Charge Traps by Stabilizing Perovskite Grain Boundary Structures: An Ab Initio Analysis with Machine Learning Force Field. *Chem. Mater.* **2024**, *36* (6), 2898–2906. <https://doi.org/10.1021/acs.chemmater.3c03261>.
- (31) Gastegger, M.; Behler, J.; Marquetand, P. Machine Learning Molecular Dynamics for the Simulation of Infrared Spectra. *Chem. Sci.* **2017**, *8* (10), 6924–6935. <https://doi.org/10.1039/C7SC02267K>.
- (32) Litman, Y.; Behler, J.; Rossi, M. Temperature Dependence of the Vibrational Spectrum of Porphycene: A Qualitative Failure of Classical-Nuclei Molecular Dynamics. *Faraday Discuss.* **2019**, *221* (0), 526–546. <https://doi.org/10.1039/C9FD00056A>.
- (33) Amano, T.; Yamazaki, T.; Matsumura, N.; Yoshimoto, Y.; Tsuneyuki, S. Transferability of the Chemical Bond-Based Machine Learning Model for Dipole Moment: The GHz to THz Dielectric Properties of Liquid Propylene Glycol and Polypropylene Glycol. arXiv October 30, 2024. <https://doi.org/10.48550/arXiv.2410.22718>.
- (34) Butler, P. W. V.; Hafizi, R.; Day, G. M. Machine-Learned Potentials by Active Learning from Organic Crystal Structure Prediction Landscapes. *J. Phys. Chem. A* **2024**, *128* (5), 945–957. <https://doi.org/10.1021/acs.jpca.3c07129>.

- (35) Morawietz, T.; Singraber, A.; Dellago, C.; Behler, J. How van Der Waals Interactions Determine the Unique Properties of Water. *Proc. Natl. Acad. Sci. U.S.A.* **2016**, *113* (30), 8368–8373. <https://doi.org/10.1073/pnas.1602375113>.
- (36) Schran, C.; Thiemann, F. L.; Rowe, P.; Müller, E. A.; Marsalek, O.; Michaelides, A. Machine Learning Potentials for Complex Aqueous Systems Made Simple. *Proc. Natl. Acad. Sci. USA* **2021**, *118* (38), e2110077118. <https://doi.org/10.1073/PNAS.2110077118>.
- (37) Yao, N.; Chen, X.; Fu, Z.-H.; Zhang, Q. Applying Classical, Ab Initio, and Machine-Learning Molecular Dynamics Simulations to the Liquid Electrolyte for Rechargeable Batteries. *Chem. Rev.* **2022**, *122* (12), 10970–11021. <https://doi.org/10.1021/acs.chemrev.1c00904>.
- (38) Dajnowicz, S.; Agarwal, G.; Stevenson, J. M.; Jacobson, L. D.; Ramezanghorbani, F.; Leswing, K.; Friesner, R. A.; Halls, M. D.; Abel, R. High-Dimensional Neural Network Potential for Liquid Electrolyte Simulations. *J. Phys. Chem. B* **2022**, *126* (33), 6271–6280. <https://doi.org/10.1021/acs.jpcb.2c03746>.
- (39) Mohanty, S.; Stevenson, J.; Browning, A. R.; Jacobson, L.; Leswing, K.; Halls, M. D.; Afzal, M. A. F. Development of Scalable and Generalizable Machine Learned Force Field for Polymers. *Sci. Rep.* **2023**, *13* (1), 17251. <https://doi.org/10.1038/s41598-023-43804-5>.
- (40) Jinnouchi, R.; Minami, S.; Karsai, F.; Verdi, C.; Kresse, G. Proton Transport in Perfluorinated Ionomer Simulated by Machine-Learned Interatomic Potential. *J. Phys. Chem. Lett.* **2023**, *14* (14), 3581–3588. <https://doi.org/10.1021/acs.jpcllett.3c00293>.
- (41) Chahal, R.; Toomey, M. D.; Kearney, L. T.; Sedova, A.; Damron, J. T.; Naskar, A. K.; Roy, S. Deep-Learning Interatomic Potential Connects Molecular Structural Ordering to the Macroscale Properties of Polyacrylonitrile. *ACS Appl. Mater. Interfaces* **2024**, *16* (28), 36878–36891. <https://doi.org/10.1021/acsami.4c04491>.
- (42) Wan, K.; He, J.; Shi, X. Construction of High Accuracy Machine Learning Interatomic Potential for Surface/Interface of Nanomaterials—A Review. *Adv. Mater.* **2023**, *36* (22), 2305758. <https://doi.org/10.1002/adma.202305758>.
- (43) Zhou, Y.; Ouyang, Y.; Zhang, Y.; Li, Q.; Wang, J. Machine Learning Assisted Simulations of Electrochemical Interfaces: Recent Progress and Challenges. *J. Phys. Chem. Lett.* **2023**, *14* (9), 2308–2316. <https://doi.org/10.1021/acs.jpcllett.2c03288>.
- (44) Stocker, S.; Gasteiger, J.; Becker, F.; Günnemann, S.; Margraf, J. T. How Robust Are Modern Graph Neural Network Potentials in Long and Hot Molecular Dynamics Simulations? *Mach. Learn.: Sci. Technol.* **2022**, *3* (4), 045010. <https://doi.org/10.1088/2632-2153/AC9955>.
- (45) Fu, X.; Wu, Z.; Wang, W.; Xie, T.; Keten, S.; Gomez-Bombarelli, R.; Jaakkola, T. Forces Are Not Enough: Benchmark and Critical Evaluation for Machine Learning Force Fields with Molecular Simulations. arXiv August 26, 2023. <https://doi.org/10.48550/arXiv.2210.07237>.
- (46) Magdău, I.-B.; Arismendi-Arrieta, D. J.; Smith, H. E.; Grey, C. P.; Hermansson, K.; Csányi, G. Machine Learning Force Fields for Molecular Liquids: Ethylene Carbonate/Ethyl Methyl Carbonate Binary Solvent. *npj Comput. Mater.* **2023**, *9*, 146. <https://doi.org/10.1038/s41524-023-01100-w>.
- (47) Matsumura, N.; Yoshimoto, Y.; Yamazaki, T.; Amano, T.; Noda, T.; Ebata, N.; Kasano, T.; Sakai, Y. A Generator of Neural Network Potential for Molecular Dynamics: Constructing Robust and Accurate Potentials with Active Learning for Nanosecond-Scale Simulations. arXiv November 26, 2024. <https://doi.org/10.48550/arXiv.2411.17191>.
- (48) Sakai, Y.; Matsumura, N.; Inoue, A.; Kawaguchi, H.; Thang, D.; Ishikawa, A.; Höskuldsson, Á. B.; Skúlason, E. Active Learning for Graph Neural Networks Training in

- Catalyst Energy Prediction. In *2024 International Joint Conference on Neural Networks (IJCNN)*; 2024; pp 1–8. <https://doi.org/10.1109/IJCNN60899.2024.10650978>.
- (49) Kusoglu, A.; Weber, A. Z. New Insights into Perfluorinated Sulfonic-Acid Ionomers. *Chem. Rev.* **2017**, *117* (3), 987–1104. <https://doi.org/10.1021/acs.chemrev.6b00159>.
 - (50) Choe, Y.-K.; Tsuchida, E.; Ikeshoji, T.; Yamakawa, S.; Hyodo, S. Nature of Proton Dynamics in a Polymer Electrolyte Membrane, Nafion: A First-Principles Molecular Dynamics Study. *Phys. Chem. Chem. Phys.* **2009**, *11* (20), 3892–3899. <https://doi.org/10.1039/B819535H>.
 - (51) Devanathan, R.; Idupulapati, N.; Baer, M. D.; Mundy, C. J.; Dupuis, M. Ab Initio Molecular Dynamics Simulation of Proton Hopping in a Model Polymer Membrane. *J. Phys. Chem. B* **2013**, *117* (51), 16522–16529. <https://doi.org/10.1021/jp410229u>.
 - (52) Hayashi, Y.; Shiomi, J.; Morikawa, J.; Yoshida, R. RadonPy: Automated Physical Property Calculation Using All-Atom Classical Molecular Dynamics Simulations for Polymer Informatics. *npj Comput. Mater.* **2022**, *8*, 222. <https://doi.org/10.1038/s41524-022-00906-4>.
 - (53) Stukowski, A. Visualization and Analysis of Atomistic Simulation Data with OVITO—the Open Visualization Tool. *Model. Simul. Mater. Sci. Eng.* **2010**, *18* (1), 015012. <https://doi.org/10.1088/0965-0393/18/1/015012>.
 - (54) Giannozzi, P.; Andreussi, O.; Brumme, T.; Bunau, O.; Buongiorno Nardelli, M.; Calandra, M.; Car, R.; Cavazzoni, C.; Ceresoli, D.; Cococcioni, M.; Colonna, N.; Carnimeo, I.; Dal Corso, A.; de Gironcoli, S.; Delugas, P.; DiStasio, R. A.; Ferretti, A.; Floris, A.; Fratesi, G.; Fugallo, G.; Gebauer, R.; Gerstmann, U.; Giustino, F.; Gorni, T.; Jia, J.; Kawamura, M.; Ko, H.-Y.; Kokalj, A.; Küçükbenli, E.; Lazzeri, M.; Marsili, M.; Marzari, N.; Mauri, F.; Nguyen, N. L.; Nguyen, H.-V.; Otero-de-la-Roza, A.; Paulatto, L.; Poncé, S.; Rocca, D.; Sabatini, R.; Santra, B.; Schlipf, M.; Seitsonen, A. P.; Smogunov, A.; Timrov, I.; Thonhauser, T.; Umari, P.; Vast, N.; Wu, X.; Baroni, S. Advanced Capabilities for Materials Modelling with Quantum ESPRESSO. *J. Phys. Condens. Matter* **2017**, *29* (46), 465901. <https://doi.org/10.1088/1361-648X/aa8f79>.
 - (55) Giannozzi, P.; Baseggio, O.; Bonfà, P.; Brunato, D.; Car, R.; Carnimeo, I.; Cavazzoni, C.; de Gironcoli, S.; Delugas, P.; Ferrari Ruffino, F.; Ferretti, A.; Marzari, N.; Timrov, I.; Urru, A.; Baroni, S. Quantum ESPRESSO toward the Exascale. *J. Chem. Phys.* **2020**, *152* (15), 154105. <https://doi.org/10.1063/5.0005082>.
 - (56) Perdew, J. P.; Burke, K.; Ernzerhof, M. Generalized Gradient Approximation Made Simple. *Phys. Rev. Lett.* **1996**, *77* (18), 3865–3868. <https://doi.org/10.1103/PhysRevLett.77.3865>.
 - (57) Zhang, Y.; Yang, W. Comment on “Generalized Gradient Approximation Made Simple.” *Phys. Rev. Lett.* **1998**, *80* (4), 890–890. <https://doi.org/10.1103/PhysRevLett.80.890>.
 - (58) Grimme, S.; Antony, J.; Ehrlich, S.; Krieg, H. A Consistent and Accurate Ab Initio Parametrization of Density Functional Dispersion Correction (DFT-D) for the 94 Elements H–Pu. *J. Chem. Phys.* **2010**, *132* (15), 154104. <https://doi.org/10.1063/1.3382344>.
 - (59) Kresse, G.; Joubert, D. From Ultrasoft Pseudopotentials to the Projector Augmented-Wave Method. *Phys. Rev. B* **1999**, *59* (3), 1758–1775. <https://doi.org/10.1103/PhysRevB.59.1758>.
 - (60) Berendsen, H. J. C.; Postma, J. P. M.; van Gunsteren, W. F.; DiNola, A.; Haak, J. R. Molecular Dynamics with Coupling to an External Bath. *J. Chem. Phys.* **1984**, *81* (8), 3684–3690. <https://doi.org/10.1063/1.448118>.
 - (61) Zeng, J.; Zhang, D.; Lu, D.; Mo, P.; Li, Z.; Chen, Y.; Rynik, M.; Huang, L.; Li, Z.; Shi, S.; Wang, Y.; Ye, H.; Tuo, P.; Yang, J.; Ding, Y.; Li, Y.; Tisi, D.; Zeng, Q.; Bao, H.; Xia, Y.; Huang, J.; Muraoka, K.; Wang, Y.; Chang, J.; Yuan, F.; Bore, S. L.; Cai, C.; Lin, Y.; Wang,

- B.; Xu, J.; Zhu, J.-X.; Luo, C.; Zhang, Y.; Goodall, R. E. A.; Liang, W.; Singh, A. K.; Yao, S.; Zhang, J.; Wentzcovitch, R.; Han, J.; Liu, J.; Jia, W.; York, D. M.; E, W.; Car, R.; Zhang, L.; Wang, H. DeePMD-Kit v2: A Software Package for Deep Potential Models. *J. Chem. Phys.* **2023**, *159* (5), 054801. <https://doi.org/10.1063/5.0155600>.
- (62) He, K.; Zhang, X.; Ren, S.; Sun, J. Identity Mappings in Deep Residual Networks. In *Computer Vision – ECCV 2016*; Leibe, B., Matas, J., Sebe, N., Welling, M., Eds.; Springer International Publishing: Cham, 2016; pp 630–645. https://doi.org/10.1007/978-3-319-46493-0_38.
- (63) Kingma, D. P.; Ba, J. Adam: A Method for Stochastic Optimization. arXiv January 30, 2017. <https://doi.org/10.48550/arXiv.1412.6980>.
- (64) Zhang, Y.; Wang, H.; Chen, W.; Zeng, J.; Zhang, L.; Wang, H.; E, W. DP-GEN: A Concurrent Learning Platform for the Generation of Reliable Deep Learning Based Potential Energy Models. *Comput. Phys. Commun.* **2020**, *253*, 107206. <https://doi.org/10.1016/j.cpc.2020.107206>.
- (65) Nosé, S. A Unified Formulation of the Constant Temperature Molecular Dynamics Methods. *J. Chem. Phys.* **1984**, *81* (1), 511–519. <https://doi.org/10.1063/1.447334>.
- (66) Hoover, W. G. Canonical Dynamics: Equilibrium Phase-Space Distributions. *Phys. Rev. A* **1985**, *31* (3), 1695–1697. <https://doi.org/10.1103/PhysRevA.31.1695>.
- (67) Parrinello, M.; Rahman, A. Polymorphic Transitions in Single Crystals: A New Molecular Dynamics Method. *J. Appl. Phys.* **1981**, *52* (12), 7182–7190. <https://doi.org/10.1063/1.328693>.
- (68) Martyna, G. J.; Tobias, D. J.; Klein, M. L. Constant Pressure Molecular Dynamics Algorithms. *J. Chem. Phys.* **1994**, *101* (5), 4177–4189. <https://doi.org/10.1063/1.467468>.
- (69) Thompson, A. P.; Aktulga, H. M.; Berger, R.; Bolintineanu, D. S.; Brown, W. M.; Crozier, P. S.; in 't Veld, P. J.; Kohlmeyer, A.; Moore, S. G.; Nguyen, T. D.; Shan, R.; Stevens, M. J.; Tranchida, J.; Trott, C.; Plimpton, S. J. LAMMPS - a Flexible Simulation Tool for Particle-Based Materials Modeling at the Atomic, Meso, and Continuum Scales. *Comput. Phys. Commun.* **2022**, *271*, 108171. <https://doi.org/10.1016/j.cpc.2021.108171>.
- (70) Shimizu, K.; Arguelles, E. F.; Li, W.; Ando, Y.; Minamitani, E.; Watanabe, S. Phase Stability of Au-Li Binary Systems Studied Using Neural Network Potential. *Phys. Rev. B* **2021**, *103* (9), 094112. <https://doi.org/10.1103/PhysRevB.103.094112>.
- (71) Narayan, A.; Berger, B.; Cho, H. Assessing Single-Cell Transcriptomic Variability through Density-Preserving Data Visualization. *Nat. Biotechnol.* **2021**, *39* (6), 765–774. <https://doi.org/10.1038/s41587-020-00801-7>.
- (72) Ziegler, J. F.; Biersack, J. P.; Littmark, U. *The Stopping and Range of Ions in Matter*; Pergamon, 1985; Vol. 1.
- (73) Morris, D. R.; Sun, X. Water-Sorption and Transport Properties of Nafion 117 H. *J. Appl. Polym. Sci.* **1993**, *50* (8), 1445–1452. <https://doi.org/10.1002/app.1993.070500816>.
- (74) Hammer, B.; Hansen, L. B.; Nørskov, J. K. Improved Adsorption Energetics within Density-Functional Theory Using Revised Perdew-Burke-Ernzerhof Functionals. *Phys. Rev. B* **1999**, *59* (11), 7413–7421. <https://doi.org/10.1103/PhysRevB.59.7413>.
- (75) Allen, M. P.; Tildesley, D. J. *Computer Simulation of Liquids*; Clarendon Press: New York, 1989.
- (76) Zawodzinski, T. A. Jr.; Neeman, M.; Sillerud, L. O.; Gottesfeld, S. Determination of Water Diffusion Coefficients in Perfluorosulfonate Ionomeric Membranes. *J. Phys. Chem.* **1991**, *95* (15), 6040–6044. <https://doi.org/10.1021/j100168a060>.

- (77) Ochi, S.; Kamishima, O.; Mizusaki, J.; Kawamura, J. Investigation of Proton Diffusion in Nafion®117 Membrane by Electrical Conductivity and NMR. *Solid State Ion.* **2009**, *180* (6), 580–584. <https://doi.org/10.1016/j.ssi.2008.12.035>.

Supporting Information

Large-Scale, Long-Time Atomistic Simulations of Proton Transport in Polymer Electrolyte Membranes Using a Neural Network Interatomic Potential

Yuta Yoshimoto, Naoki Matsumura, Yuto Iwasaki, Hiroshi Nakao, and Yasufumi Sakai*

Fujitsu Research, Fujitsu Limited, 4-1-1 Kamikodanaka, Nakahara-ku, Kawasaki, Kanagawa
211-8588, Japan

S1. Methods for Constructing Nafion Systems

This section describes the procedure for generating initial structures for the Nafion systems. Section S1.1 details how to construct initial structures for NNP training, while Section S1.2 describes how to construct initial structures for large-scale simulations. The Nafion systems are generated using RadonPy.¹

S1.1. Construction of Initial Structures for NNP Training.

Initial Structure of the Dry Nafion System. Initially, 1,000 3D conformations of the Nafion monomer are generated from its SMILES string using RDKit. These conformations are then subjected to molecular mechanics optimization using the modified GAFF2 force field parameterized for fluorocarbons.² Subsequently, density functional theory (DFT) calculations using the PSI4 software³ are performed to optimize the four most stable structures obtained from the molecular mechanics calculations. These DFT calculations employ the ω B97M-D3BJ functional^{4,5} and the 6-31G(d,p) basis set. For the lowest energy structure, a single-point calculation using the Hartree–Fock method with the 6-31G(d) basis set is performed to obtain restrained electrostatic potential (RESP) charges.⁶ Four Nafion monomers, assigned with the derived atomic charges and the modified GAFF2 parameters, are then placed in a simulation box with a target density of 0.2 g/cm³. A heating simulation is performed in the NVT ensemble from 400 K to 700 K over 1 ns, using a 1-fs timestep size and the Nosé–Hoover thermostat^{7,8} with a time constant of 100 fs. All bond lengths and angles involving hydrogen atoms are constrained using the RATTLE algorithm.⁹ The system is then isotropically compressed to a density of 0.8 g/cm³ over 1 ns at 700 K in the NVT ensemble. This is followed by a 21-step compression/decompression equilibration run¹⁰ for 1.5 ns. Finally, a 20-ns equilibration is

performed in the NPT ensemble at 400 K and 1 bar, using the Nosé–Hoover style thermostat^{7,8} and barostat^{11,12} with time constants of 100 fs and 1000 fs, respectively.

Initial Structures of the Hydrated Nafion Systems. Modified GAFF2 parameters² and RESP charges are assigned to the Nafion monomers using the same procedure as that employed for the dry Nafion system. For the hydrated systems with the hydration levels $\lambda = 1$ and 7, three Nafion monomers are placed in a simulation box with a target density of 0.2 g/cm³, followed by the random insertion of 3 and 21 water molecules, respectively. For the system with $\lambda = 13$, two Nafion monomers are placed in the box at a target density of 0.2 g/cm³, and 26 water molecules are randomly inserted. The TIP3P model¹³ is used for water. The system is then isotropically compressed to a density of 1.0 g/cm³ over 5 ns at 700 K in the NVT ensemble. A 21-step compression/decompression equilibration¹⁰ is then performed for 1.5 ns. Finally, a 20-ns equilibration is conducted in the NPT ensemble at 400 K and 1 bar.

Initial Structure of the Water System. Thirty-two water molecules are randomly placed in a simulation box with a target density of 0.5 g/cm³. The TIP3P model¹³ is employed for water. The system is then cooled from 1000 K to 353 K over 1 ns in the NVT ensemble using a 1-fs time step and the Nosé–Hoover thermostat with a time constant of 100 fs. The O–H bond lengths and H–O–H bond angles are constrained using the RATTLE algorithm.⁹ Subsequently, a 1-ns equilibration is performed in the NPT ensemble at 353 K and 1 bar, using the Nosé–Hoover style thermostat and barostat with time constants of 100 fs and 1000 fs, respectively.

S.1.2. Construction of Initial Structures for Large-Scale Simulations.

Initial Structure of the Dry Nafion System. RESP charges are assigned to the Nafion monomer following the procedure detailed in Section S.1.1. Subsequently, a Nafion 14-mer is generated using the polymerization functionality of RadonPy¹ and assigned with the modified GAFF2 parameters.² Ten 14-mers are then randomly placed in a simulation box, targeting a density of 0.2 g/cm³. The subsequent equilibration procedure is identical to that described in Section S.1.1.

Initial Structures of the Hydrated Nafion Systems. The procedure for placing ten Nafion 14-mers in the simulation box is identical to that employed for the dry Nafion system. Subsequently, 420, 840, 1,680, 2,520, and 3,360 water molecules are randomly inserted into the simulation boxes to generate hydrated systems with $\lambda = 3, 6, 12, 18,$ and 24 , respectively. The subsequent equilibration procedure is identical to that detailed in Section S.1.1.

S2. Stability of NNP-MD Simulations of Large Systems

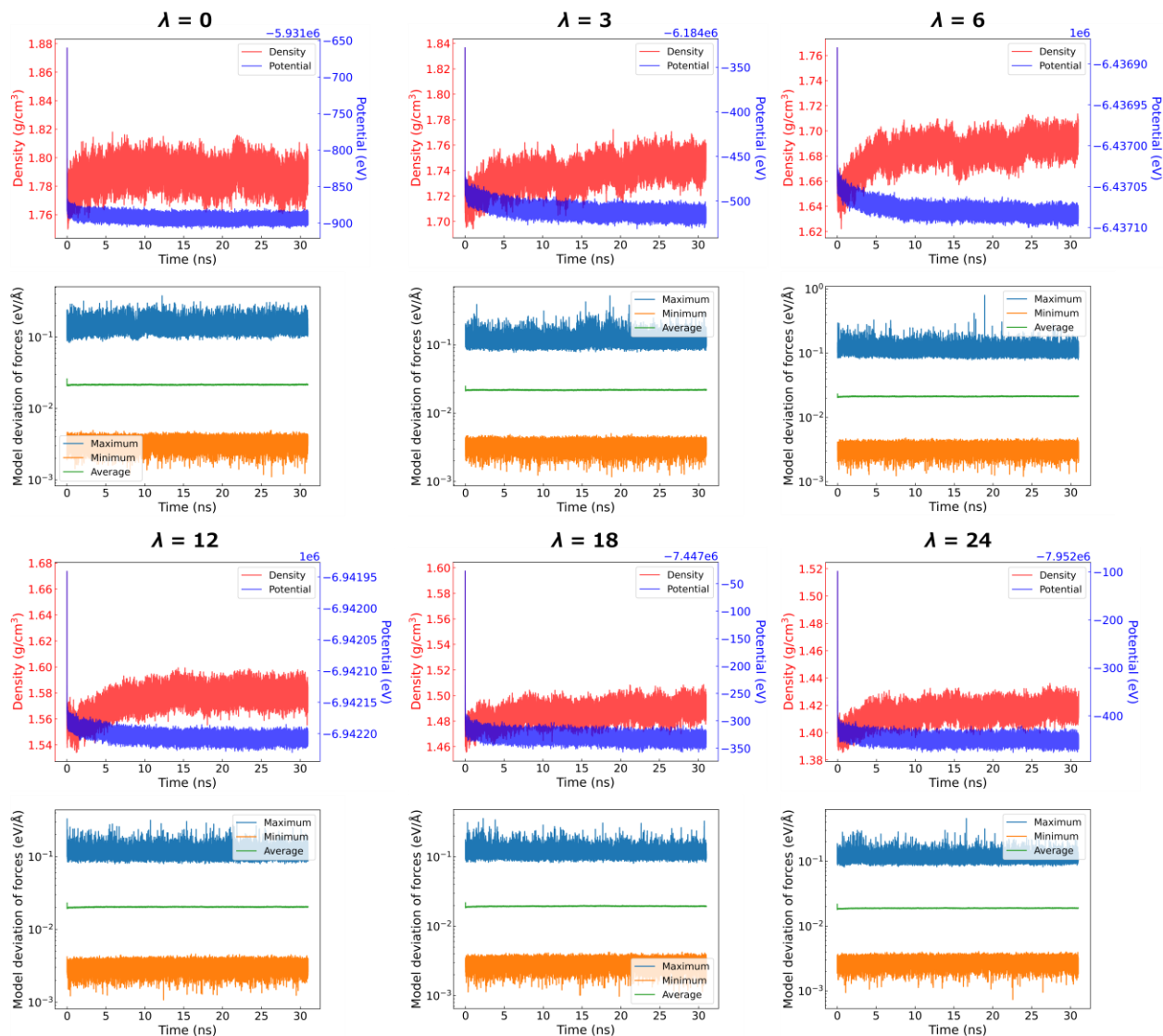


Figure S1. Temporal changes in the densities, potential energies, and model deviations of forces for the Nafion systems with $\lambda = 0, 3, 6, 12, 18, \text{ and } 24$ simulated using the DP-iter-17 model. The model deviations of forces are calculated for all the atoms and their maximum, minimum, and average values are presented.

REFERENCES

- (1) Hayashi, Y.; Shiomi, J.; Morikawa, J.; Yoshida, R. RadonPy: Automated Physical Property Calculation Using All-Atom Classical Molecular Dynamics Simulations for Polymer Informatics. *npj Comput. Mater.* **2022**, *8*, 222. <https://doi.org/10.1038/s41524-022-00906-4>.
- (2) Träg, J.; Zahn, D. Improved GAFF2 Parameters for Fluorinated Alkanes and Mixed Hydro- and Fluorocarbons. *J. Mol. Model.* **2019**, *25* (2), 39. <https://doi.org/10.1007/s00894-018-3911-5>.
- (3) Smith, D. G. A.; Burns, L. A.; Simmonett, A. C.; Parrish, R. M.; Schieber, M. C.; Galvelis, R.; Kraus, P.; Kruse, H.; Di Remigio, R.; Alenaizan, A.; James, A. M.; Lehtola, S.; Misiewicz, J. P.; Scheurer, M.; Shaw, R. A.; Schriber, J. B.; Xie, Y.; Glick, Z. L.; Sirianni, D. A.; O'Brien, J. S.; Waldrop, J. M.; Kumar, A.; Hohenstein, E. G.; Pritchard, B. P.; Brooks, B. R.; Schaefer, H. F., III; Sokolov, A. Yu.; Patkowski, K.; DePrince, A. E., III; Bozkaya, U.; King, R. A.; Evangelista, F. A.; Turney, J. M.; Crawford, T. D.; Sherrill, C. D. PSI4 1.4: Open-Source Software for High-Throughput Quantum Chemistry. *J. Chem. Phys.* **2020**, *152* (18), 184108. <https://doi.org/10.1063/5.0006002>.
- (4) Mardirossian, N.; Head-Gordon, M. ω B97M-V: A Combinatorially Optimized, Range-Separated Hybrid, Meta-GGA Density Functional with VV10 Nonlocal Correlation. *J. Chem. Phys.* **2016**, *144* (21), 214110. <https://doi.org/10.1063/1.4952647>.
- (5) Grimme, S.; Ehrlich, S.; Goerigk, L. Effect of the Damping Function in Dispersion Corrected Density Functional Theory. *J. Comput. Chem.* **2011**, *32* (7), 1456–1465. <https://doi.org/10.1002/jcc.21759>.
- (6) Bayly, C. I.; Cieplak, P.; Cornell, W. D.; Kollman, P. A. A Well-Behaved Electrostatic Potential Based Method Using Charge Restraints for Deriving Atomic Charges: The RESP Model. *J. Phys. Chem.* **1993**, *97* (40), 10269–10280. <https://doi.org/10.1021/j100142a004>.
- (7) Nosé, S. A Unified Formulation of the Constant Temperature Molecular Dynamics Methods. *J. Chem. Phys.* **1984**, *81* (1), 511–519. <https://doi.org/10.1063/1.447334>.
- (8) Hoover, W. G. Canonical Dynamics: Equilibrium Phase-Space Distributions. *Phys. Rev. A* **1985**, *31* (3), 1695–1697. <https://doi.org/10.1103/PhysRevA.31.1695>.
- (9) Andersen, H. C. Rattle: A “Velocity” Version of the Shake Algorithm for Molecular Dynamics Calculations. *J. Comput. Phys.* **1983**, *52* (1), 24–34. [https://doi.org/10.1016/0021-9991\(83\)90014-1](https://doi.org/10.1016/0021-9991(83)90014-1).
- (10) Larsen, G. S.; Lin, P.; Hart, K. E.; Colina, C. M. Molecular Simulations of PIM-1-like Polymers of Intrinsic Microporosity. *Macromolecules* **2011**, *44* (17), 6944–6951. <https://doi.org/10.1021/ma200345v>.
- (11) Parrinello, M.; Rahman, A. Polymorphic Transitions in Single Crystals: A New Molecular Dynamics Method. *J. Appl. Phys.* **1981**, *52* (12), 7182–7190. <https://doi.org/10.1063/1.328693>.
- (12) Martyna, G. J.; Tobias, D. J.; Klein, M. L. Constant Pressure Molecular Dynamics Algorithms. *J. Chem. Phys.* **1994**, *101* (5), 4177–4189. <https://doi.org/10.1063/1.467468>.
- (13) Jorgensen, W. L.; Chandrasekhar, J.; Madura, J. D.; Impey, R. W.; Klein, M. L. Comparison of Simple Potential Functions for Simulating Liquid Water. *J. Chem. Phys.* **1983**, *79* (2), 926–935. <https://doi.org/10.1063/1.445869>.